Improving the Electrochemical Performances of Li-rich $Li_{1.20}Ni_{0.13}Co_{0.13}Mn_{0.54}O_2$ through a Cooperative Doping of Na^+ and PO_4^{3-} with Na_3PO_4

Yi Liu [a], De Ning[b], Lirong Zheng[c], Rui Gao[a], Jicheng Zhang[a], Alexandra Franz[b], Gerhard Schumacher[b], Zhongbo Hu[a], and Xiangfeng Liu[a]*

[a] College of Materials Science and Opto-Electronic Technology, University of Chinese Academy of Sciences, Beijing 100049, PR China

[b] Helmholtz-Center Berlin for Materials and Energy, Hahn-Meitner-Platz 1, 14109 Berlin, Germany
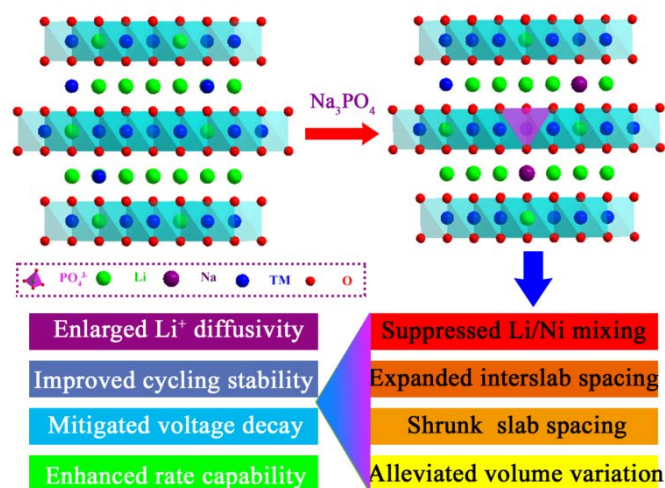
[c] Beijing Synchrotron Radiation Facility, Institute of High Energy Physics, Chinese Academy of Sciences, Beijing 100049, China

Corresponding E-mail: liuxf@ucas.ac.cn

Abstract

Li-rich layered oxide cathodes attract much attention as one of the most promising cathode materials for the next generation lithium-ion batteries due to the high theory capacity. But they suffer from the poor rate capability, voltage decay and the inferior cycling stability. Herein, we propose a novel synergistic strategy to improve the electrochemical performances of Li-rich $Li_{1.20}Ni_{0.13}Co_{0.13}Mn_{0.54}O_2$ cathode by the co-doping of Na^+ and PO_4^{3-}. The simultaneous doping of Na^+ for Li sites and PO_4^{3-} for Mn sites has been achieved using Na_3PO_4 as a dopant. The Na^+ and PO_4^{3-} co-doped sample show the enhanced high-rate performance (106.4 $mAhg^{-1}$@10C), excellent capacity retention (93.8%@1C@100 cycles) and the mitigated voltage decay owing to the synergistic effect of Na^+ and PO_4^{3-} co-doping. The synergistic mechanism has been examined by means of neutron diffraction, X-ray photoelectron spectroscopy, *ex-situ* X-ray absorption spectra and *ex-situ* X-ray diffraction. The co-doping of Na^+ and PO_4^{3-} largely enlarges the interlayer spacing and suppresses the Li/Ni mixing which increases Li^+ diffusivity and enhances the rate capability. Meanwhile, the co-doping of Na^+ and PO_4^{3-} shrinks the thickness of the slabs, weakens the TM-O covalency and alleviates the volume change in the charge/discharge process which are favorable to the layered structure stability and the cycling performances. This study presents some new insights into the improvement mechanism of foreign elements doping which is instructive to design high performance cathode materials through a cooperative modulation of different crystal sites doping.

TOC

The simultaneous doping of Na^+ and PO_4^{3-} for Li and Mn has been achieved using Na_3PO_4 as a dopant. The co-doping of Na^+ and PO_4^{3-} enlarges the interlayer spacing and suppresses the Li/Ni mixing which increases Li^+ diffusivity and enhances the rate capability. Meanwhile, the co-doping of Na^+ and PO_4^{3-} shrinks the thickness of the slabs and alleviates the volume change in the charge/discharge process which is favorable for the layered structure stability and the cycling performances.

Introduction

Lithium-ion batteries (LIBs) have been widely used in portable devices (laptops, smartphones and so on) and also show a great potential in electric vehicles (EV) [1-6]. Layered transition metal oxides with a general formula $LiTMO_2$(TM = Ni, Co, or Ni/Co/Mn) are the most widely used positive materials in commercial LIBs[7] due to their high operating voltage and relatively high specific capacity of 140-180 mAh g^{-1}. However, the traditional cathode materials with moderate specific capacities are insufficient to meet the demanding requirements in electric vehicles or hybrid electric vehicles. Hence, it's a big challenge to explore the new generation of high energy density cathode materials. The lithium-rich Mn-based layered oxide with a general formula $xLi_2MnO_3 \cdot (1-x)LiTMO_2$(TM=Mn, Ni, Co), is one of the most promising candidates due to the high reversible capacity (~300 mAhg^{-1}) which is almost twice as high as the commercial $LiCoO_2$ and $LiFePO_4$[8-10]. The lithium-rich Mn-based oxides are reported as two different phases integrated at the scale in the oxide grains: one with a monoclinic Li_2MnO_3-like layered structure (C/2m) and the other with a rhombohedral $LiTMO_2$ ($R\bar{3}m$)[11]. These materials can achieve such a high specific capacity because the component of Li_2MnO_3 phase serves as an active phase when the charging potential is higher than 4.5 V versus Li/Li^{+}[12-14]. However, the lithium-rich Mn-based oxides cathodes still suffer from the critical issues: (1) low initial Coulombic efficiency in the first cycle caused by the release of oxygen and the irreversible removal of Li_2O from its crystal lattice; (2) poor rate capability which is mainly caused by the low e^{-} and Li^{+} conductivity; (3) poor cycling stability and (4) critical voltage decay during the cycling

process[15, 16].

A few modification approaches have been employed to relieve these problems. The elements doping is an effective method, and the foreign cations[17-20] (such as Mg, Zn, Al, Ti, and so on) and anions [21-24] (such as BO_4^{5-}, SiO_4^{4-}, PO_4^{3-} and so on) have been incorporated into the transition metal slab which can reduce Ni^{2+} ion migration and weaken the TM-O covalency in the oxygen closely packed structure to alleviate the voltage decay and improve the cyclic durability. In addition, surface coating with metal oxides[25], metal phosphates[26], metal fluorides[27] and so on, is another modification strategy to mitigate these unwanted issues. The coating layer protect the surface structure by suppress the side reaction between the positive electrode and the electrolyte under high voltage and it also could restrain the surface crystal structure phase transition which leads to the capacity fading.

In this work, we successfully synthesized a Na^+ and PO_4^{3-} co-doped Li-rich cathode sample using Na_3PO_4 as the dopant. The obtained Na^+ and PO_4^{3-} co-doped $Li_{1.17}Na_{0.03}Ni_{0.13}Co_{0.13}Mn_{0.53}P_{0.01}O_2$ exhibits a significantly enhanced reversible capacity, rate performance (106.4mAhg^{-1}@10C), excellent capacity retention (93.8%@1C@100 cycles) and remarkably mitigated voltage decay. The performance enhancements can be attributed to the synergistic integration of the PO_4^{3-} polyanions in the TM layer and Na^+ in the Li layer. Firstly, the cooperative doping of Na^+ and PO_4^{3-} enlarges the interslab spacing which facilitates Li-ion diffusion and subsequently promotes the high-rate capability. Secondly, the cooperative doping of Na^+ and PO_4^{3-} alleviates the Li/Ni mixing which is not only favorable to Li^+ diffusion and the rate

capability but also suppresses the phase transition and improves the layered structure stability. Thirdly, the thickness of $S_{(MO2)}$ is shortened, and the TM-O covalency is weakened by the cooperative doping of Na^+ and PO_4^{3-}, which is also favorable to stability of the layered structure and the mitigation the voltage fade. Fourthly, the volume variation of crystal lattices in charge/discharge process is also alleviated by the codoping of Na^+ and PO_4^{3-} which further benefits the stability of the layered structure and cycling performance.

2 Experimental

2.1 Materials synthesis

The precursor of $(Ni_{0.13}Co_{0.13}Mn_{0.54})_{1.25}C_2O_4 \cdot 2H_2O$ and $(Ni_{0.13}Co_{0.13}Mn_{0.53})_{1.27}C_2O_4 \cdot 2H_2O$ were synthesized via a co-precipitation method. Stoichiometric amounts of $NiSO_4 \cdot 6H_2O$, $CoSO_4 \cdot 7H_2O$ and $MnSO_4 \cdot 5H_2O$ were first dissolved in distilled water to form a 2 M mixed solution, and a small amount of $H_2C_2O_4$ water solution (1M) was dropped to the mixed solution. Then the solution was vigorously stirred at 700-1000 rpm for 12h.The obtained oxalate precursor was washed by distilled water three times and ethanol two times and dried overnight at 80 °C. A stoichiometric amount of Li_2CO_3 (5% excess) was added to these obtained two kinds of as-prepared precursor, besides, small amounts of $NH_4H_2PO_4$ or $Na_3PO_4 \cdot 12H_2O$ was separately mixed in the obtained $(Ni_{0.13}Co_{0.13}Mn_{0.53})_{1.27}C_2O_4 \cdot 2H_2O$ precursor. Then the mixtures were calcined at 500 °C for 5 h and then at 900 °C for 12 h respectively. The obtained three cathode samples of $Li_{1.20}Ni_{0.13}Co_{0.13}Mn_{0.54}O_2$, $Li_{1.20}Ni_{0.13}Co_{0.13}Mn_{0.53}P_{0.01}O_2$ and $Li_{1.17}Na_{0.03}Ni_{0.13}Co_{0.13}Mn_{0.53}P_{0.01}O_2$ were denoted as

Pristine, P-LNCM and Na3P-LNCM, respectively.

2.2 Material characterization

The crystal structures of the as-prepared samples were characterized using an X-ray diffactometer (XRD, Rigaku SmartLab CuKα) in the 2θ range of 10°-80°. Data were recorded at a step width of 0.02° and a scan rate of 10° per minute. The morphological images and detailed lattice spacing of the as prepared samples were obtained by using scanning electron microscope (SEM, Hitachi S-4800, 2kV) and high resolution transmission electron microscope (HRTEM, JEOL-2010F, 200 kV). An X-ray photoelectronic spectrometer (XPS, Thermo Scientific ESCALAB 250Xi) using non-monochromated Al Kα X-ray radiation as the excitation source was used to observe the surface element composition and the chemical environment. The spectrum was calibrated with a C1s peak (284.7 eV) before analysis. X-ray absorption spectra (XAS) were collected on the 1W1B beamline of the Beijing Synchrotron Radiation Facility (BSRF, Beijing, China). The experiments of neutron powder diffraction were performed at the research reactor BER II at Helmholtz-Zentrum Berlin für Materialien und Energie (HZB) using the fine resolution powder diffractometer FIREPOD (E9), data were collected at ambient temperature with the wavelength $\lambda = 1.7982(1)$ Å.

2.3 Electrochemical Characterization

The electrochemical performances of the samples were evaluated by using CR2025 coin cells. The active materials, carbon black and polyvinylidene fluoride (PVDF) were mixed in N-methyl-2-pyrrolidone (NMP) with a weight ratio of 8:1:1 to form a slurry. Subsequently, the slurry was spread on an aluminum foil current

uniformly and dried at 80 °C for 4 h, then heated up to 110 °C for 12h in a vacuum oven

to obtain the as-prepared cathodes. The coin-type half-cells (CR2025) were assembled

in an Ar-filled glove box. The electrolyte was LiPF6 (1 mol L^{-1}) in a mixture of ethylene

carbonate (EC)/dimethyl carbonate (DMC) with a mass ratio of 1:1. An automatic

galvanostate (Model 2001T, Land, China) was used to perform the charge-discharge

cycling between 2.0 and 4.8 V (vs. Li/Li$^+$) at different current rates. Electrochemical

impedance spectroscopy (EIS) was performed on an electrochemical workstation

(Metrohm-Autolab, PGSTAT 302N) instrument with an amplitude of 5 mV and a

frequency range from 100 kHz to 0.1 Hz. Cyclic voltammogram (CV) measurements

were also carried out on the Electrochemical Workstation (Metrohm-Autolab,

PGSTAT302N) instrument at a scan rate of 0.1 mV s^{-1} between 2.0 and 4.8 V (vs. Li/Li$^+$).
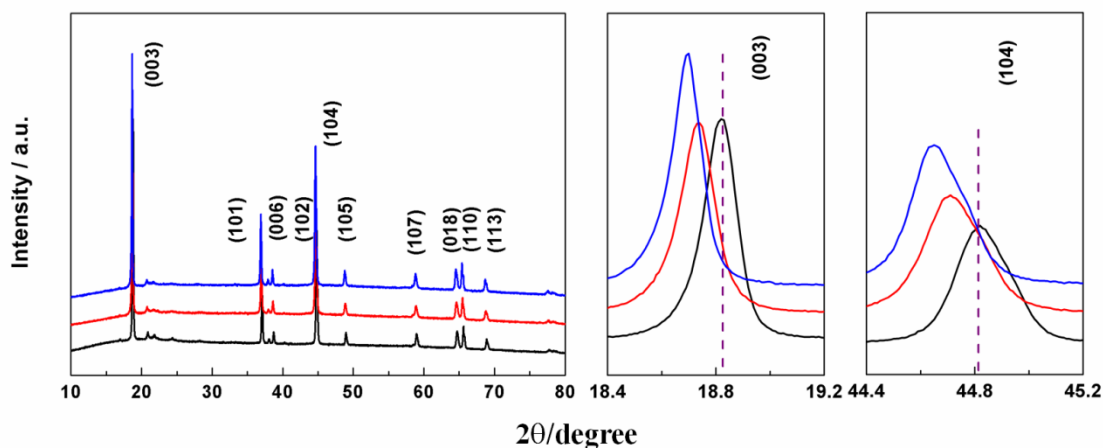
3 Results and discussion

Figure 1 XRD patterns of the Pristine (a) P-LNCMO (b) and N3P-LNCMO (c).The enlarged XRD patterns
between 18.4 to 19.2°, 44.4 to 45.2° displayed in the right side.

Figure 1 shows the XRD patterns of Pristine, P-LNCM and N3P-LNCM. All the

diffraction peaks of these samples can be well indexed to a layered α-NaFeO$_2$-type

structure with the space group of $R\bar{3}m$, and the additional weak superlatttice peaks

ranged from 20° to 25° can be identified with space group C2/m which is caused by LiMn$_6$ cation existing in the transition metal layers. XRD patterns also show the clear splitting peak of (006) and (102) near 38°, (018) and (110) near 66°, which indicates that all of these samples have a well-organized structure[28]. It is well known that a diffraction corresponding to a smaller 2θ angle in the XRD pattern has a larger interslab spacing. In the layered cathode materials, a larger interslab spacing can significantly facilitate the lithium diffusion and improve the high rate capability[29-31]. The enlarged graphs of the (003) and (104) reflections taken from the corresponding powder XRD patterns indicates that the P-LNCM and N3P-LNCM have a larger interslab spacing than the Pristine, and the N3P-LNCM has the largest interslab spacing in these three samples. This phenomenon indicates that the PO$_4^{3-}$ was introduced into the TM layer of P-LNCM sample successfully, and Na$^+$ and PO$_4^{3-}$ were co-doped into the Li layer and TM layer, respectively, in N3P-LNCM. In order to get further structure information and the interslab spacing difference of these samples, we performed the Rietveld refinement with an $R\bar{3}m$ space group. The fitting curves and the results of Rietveld refinements are shown in Fig. 2 and Table 1.
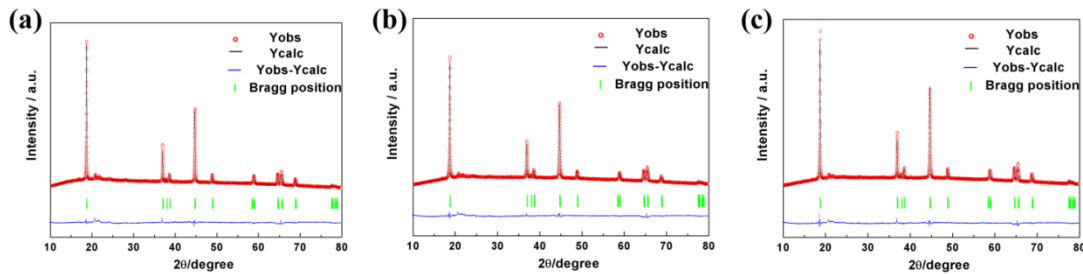

Figure 2 Observed/calculated XRD patterns of Pristine (a), P-LNCM (b) and N3P-LNCM (c)

Table 1 Cell parameters, slab thickness(S), and interslab thickness (I) for the layered phase derived from the Rietveld refinements of the as-prepared three samples

material	a[Å]	c[Å]	V[Å^3]	z_{ox}	S(Å)	I(Å)	TM-O(Å)	O-O(Å)	R_{wp}(%)
Bare	2.8452(1)	14.2075(4)	99.60(3)	0.2402(6)	2.6447	2.0912	1.948(2)	2.8452(2)	2.63

| P-LNCM | 2.8478(4) | 14.2081(5) | 99.80(5) | 0.2414(2) | 2.6119 | 2.1242 | 1.959(2) | 2.8479(4) | 2.41 |
| N3P-LNCM | 2.8489(3) | 14.2121(5) | 99.90(4) | 0.2416(6) | 2.6058 | 2.1316 | 1.960(2) | 2.8489(2) | 2.34 |

The results of Rietveld refinements show that the lattice parameters a and c of the Pristine sample is 2.8452(1) A and 14.2075(4) Å. After the PO_4^{3-} doping in the TM layer, a and c increase to 2.8478(4) Å and 14.2081(5) Å, respectively. For the Na^+ and PO_4^{3-} co-doped N3P-LNCM sample, Na^+ is doped into the Li layer and PO_4^{3-} enters the TM layer which cause the lattice parameters a and c to increase to 2.8489(3) Å and 14.2121(5) Å, respectively. The slab thickness ($S_{(MO2)}$) and interslab thickness ($I_{(LiO2)}$) of the layered structure was calculated according the two equations ($S_{(MO2)}= 2[(1/3) - z_{ox}]*c$; $I_{(LiO2)}= (c/3) - S_{(MO2)}$) reported in previous studies[32-34]. The $S_{(MO2)}$ and $I_{(LiO2)}$ value of the Pristine sample is calculated to be 2.6444 Å and 2.0912 Å. After the PO_4^{3-} was incorporated to the TM layer, the value of $S_{(MO2)}$ decreased to 2.6119 Å and the $I_{(LiO2)}$ increased to 2.1242 Å. When the Na^+ and PO_4^{3-} are co-doped into the cathode material, the $S_{(MO2)}$ value further decreased to 2.6058 Å, and the $I_{(LiO2)}$ value steadily increased to 2.1316 Å, which could be attributed to the contribution integration of the PO_4^{3-} polyanions in the TM layer and Na^+ in the interslab. The above analysis indicate that the cooperative doping of Na^+ and PO_4^{3-} enlarge the interslab spacing which facilitates Li-ion diffusion by reducing the energy barrier of the insertion/extraction, and subsequently enhances the high-rate capability. Meanwhile, the thickness of $S_{(MO2)}$ is shortened by the cooperative doping of Na^+ and PO_4^{3-}, which is favorable to stability of the layered structure. In addition, the TM-O bond length increases and the TM-O covalency decreases with the codoping of Na^+ and PO_4^{3-} which further benefit the layered structure stability.
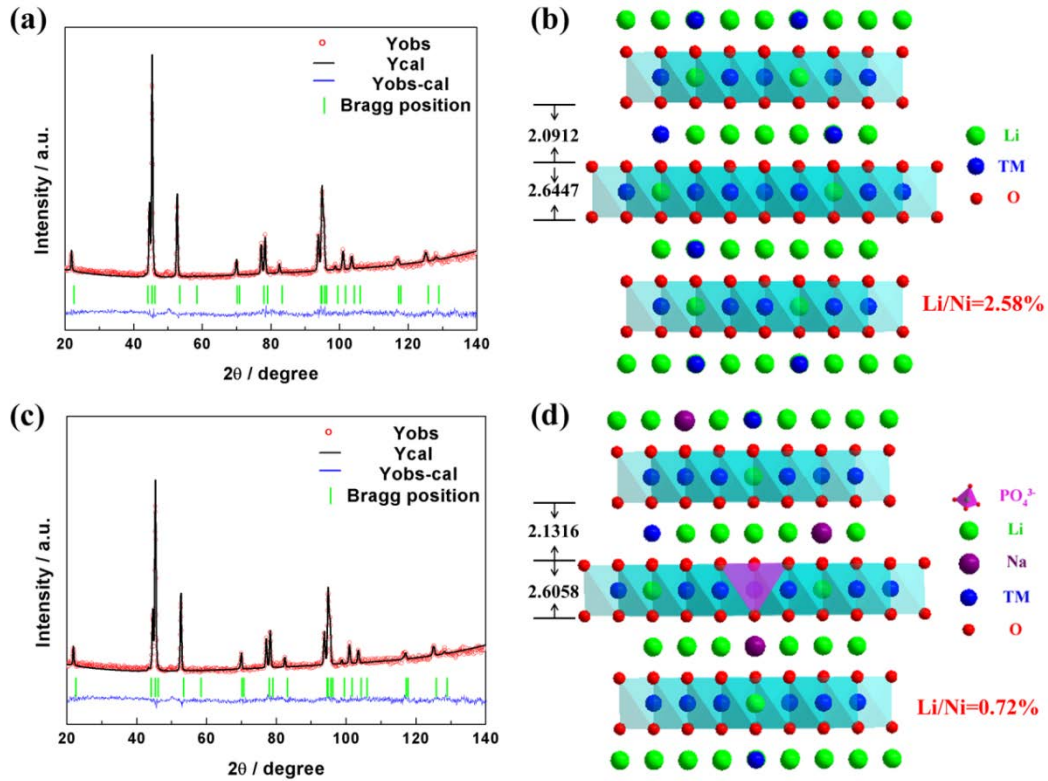
Figure 3 Rietveld refinement results of Pristine (a) and N3P-LNCM (c) using the neutron diffraction patterns measured at 25 ℃, and the corresponding Li/Ni disorder structure sketch map of Pristine (b), N3P-LNCM (d). The red circle symbols and the black line denote the observed and calculated intensities, respectively. Short green verticals indicate the positions of possible Bragg reflections. The difference between the observed and calculated profiles is plotted at the bottom. The wavelength of the incident neutrons is 1.7982(1) Å. Rietveld refinements were performed by the trigonal R-3m.

It is difficult for X-ray diffraction to distinct light weight Li, neutron diffraction were used to detect the lithium atoms occupancies combined with Rietveld refinement.[35] Owing to the similar ionic radii of Li^+ (0.72Å) and Ni^{2+} (0.69Å), a fraction of Li^+ sites are occupied by Ni^{2+} and some Ni^{2+} sites are taken by Li^+, namely, Li/Ni mixing, which blocks the lithium diffusion pathway and increases the barrier of Li^+ diffusion[36]. The neutron powder diffraction measurement is further performed to quantitatively obtain the fractions of site exchange between Li^+ and Ni^{2+} ions. Figure 3 shows Rietveld fitting results of Pristine (Figure 3a) and N3P-LNCM (Figure 3c) using the neutron diffraction patterns, and the corresponding Li/Ni disorder structure sketch map of Pristine (Figure 3b) and N3P-LNCM (Figure 3d). Figure 3(a) and (c) display

the neutron powder diffraction patterns of Pristine (a) and N3P-LNCM (c) which shows a good agreement between the experimental and calculated intensities with R_{wp} of 5.41 and 5.36%, respectively. The fitting curves and the results of Rietveld refinements are shown in Figure 3 and Table 2. The Figure 3(b) and (d) shows the Li/Ni mixing of Pristine and N3P-LNCM is 2.58% and 0.72%, respectively, indicating that the cooperative doping of Na^+ and PO_4^{3-} suppresses the Li/Ni mixing which can improve Li-ion diffusivity and the rate performance.

Table 2 The Refinement results of Pristine and N3P-LNCMO based on neutron diffraction patterns.

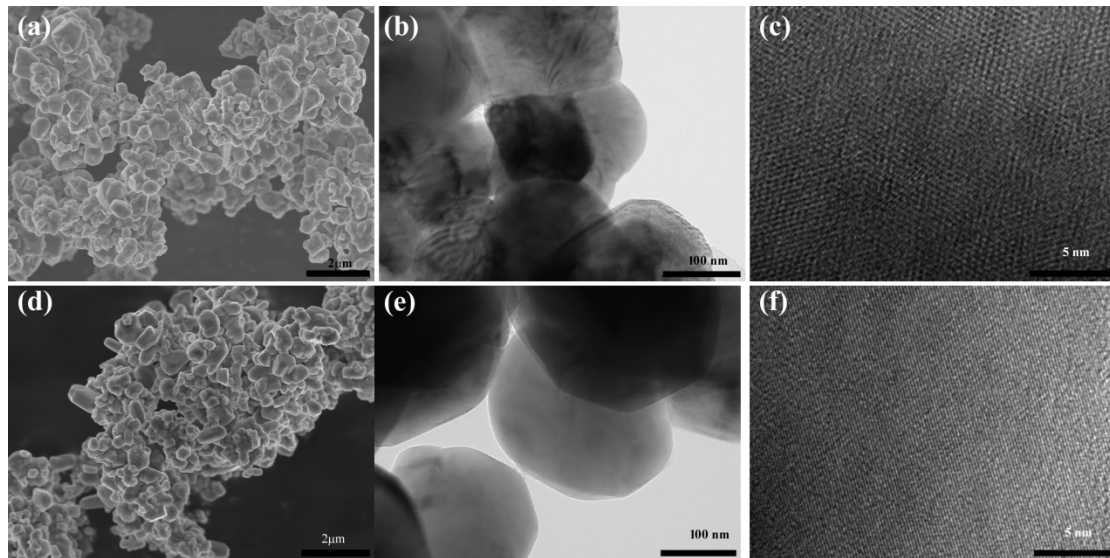| Samples		Li(3a)	Na(3a)	Ni(3a)	Li(3b)	Ni(3b)	Co(3b)	Mn(3b)	O(6c)
Pristine	x	0	0	0	0	0	0	0	0
	y	0	0	0	0	0	0	0	0
	z	0	0	0	0.5	0.5	0.5	0.5	0.242
	Occ.	0.975	0	0.025	0.225	0.105	0.130	0.540	1
N3P-LNCM	x	0	0	0	0	0	0	0	0
	y	0	0	0	0	0	0	0	0
	z	0	0	0	0.5	0.5	0.5	0.5	0.242
	Occ.	0.962	0.031	0.007	0.207	0.123	0.130	0.540	1

Figure 4 SEM images of Pristine (a) and N3P-LNCM (d). The low magnified HRTEM images of Pristine (b) and N3P-LNCM (e). The high magnification images of Pristine (c) and N3P-LNCM (f)

In order to examine the surface morphology of Pristine and N3P-LNCM, SEM and

HRTEM measurements are applied. It can be clearly seen in Figure 4a and d that both of these two samples are consisted of well-crystallized particles with similar morphologies. The low magnified HRTEM images (Figure 4b and e) could further demonstrate Pristine and N3P-LNCM samples have a uniform shape with the size range from 200 to 300 nm. Figure 3c and f shows the high magnification images of Pristine and N3P-LNCM with clear crystalline lattices.
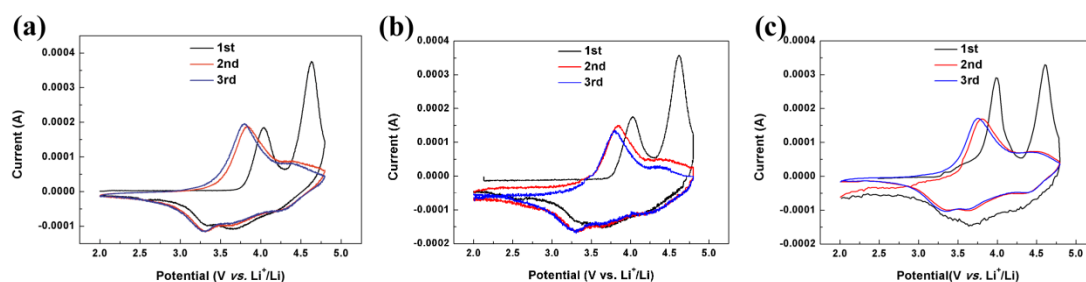

Figure 5 Cyclic voltammetry (CV) curves of Pristine (a), P-LNCM (b) and N3P-LNCM (c)

To compare the electrochemical redox response of these three samples, the cycle voltammetry (CV) measurements were carried out. Figure 5 shows the CV curves of Pristine, P-LNCM and N3P-LNCM. For the pristine sample (Figure 5a), there are two clear oxidation peaks around 3.9 V and 4.6V (*vs.* Li$^+$/Li) in the first anodic scan CV curve, which could be resulted from the oxidation of Ni^{2+} and Co^{3+} ions and the removal of Li$^+$ ions in structure accompanied with the simultaneous oxygen release, respectively[3, 37-39]. Two apparent reduction peaks around 3.7 V and 3.3 V could be clearly seen in the reversal scan, which could be attributed to the reduction of Ni^{3+} and Mn^{4+}. After two cycle CV curves, some changes appear. The strongest oxidation peak around 3.6 V in the first scan disappeared, which indicated the Li$^+$ was irreversibly removed from the crystal lattice. In contrast, the CV curves of P-LNCM and N3P-LNCM samples (Figure 5b and c) in the first cycle showed some differences with the

Pristine curve. First, the oxidation peak at 4.6 V had a slight shift that decreased from 4.63 V (Pristine) to 4.61 V (N3P-LNCM). Although these two oxidation peaks of Pristine, P-LNCM and N3P-LNCM were similar, the relative ratio of these two peaks had a apparent difference. The ratio of the oxidation peak current I(4.6V)/I(3.9V) was defined as R, and the R value for Pristine, P-LNCM and N3P-LNCM is 2.032, 2.025 and 1.131, respectively. According to a previous research[37], the oxidation peak around 4.6 V was caused by the irreversible electrochemical reaction, and the low I(4.6V)/I(3.9V) value indicates a stable structure with an alleviated oxygen loss at the high potential region, which suggests that the Na^+ and PO_4^{3-} co-doping may make less structural changes and benefit the cycling stability.
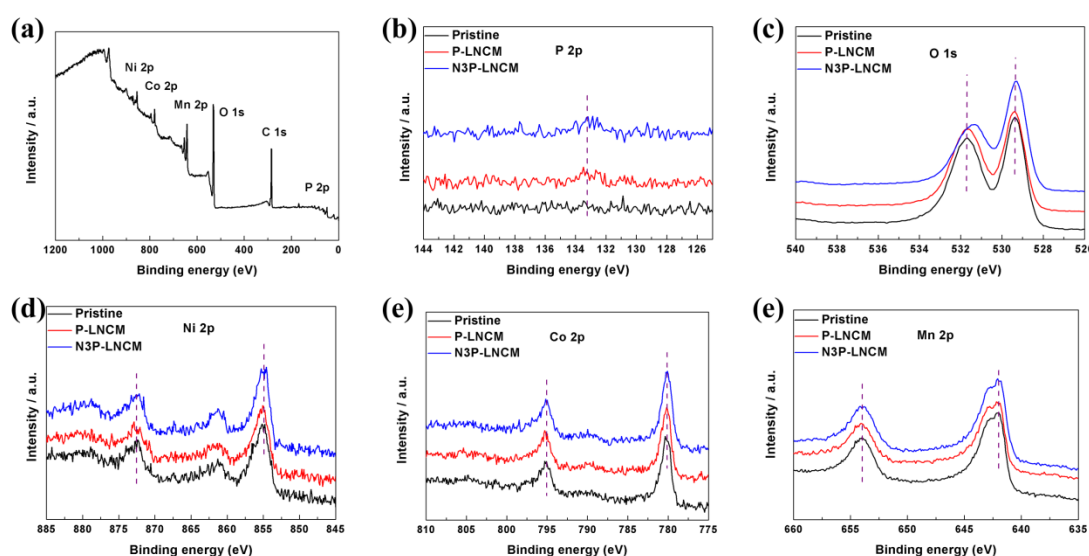

Figure 6 (a) X-ray photoelectron survey spectrum of PO_4^{3-} doped sample. X-ray photoelectron spectrum for (b) P 2p， (c) O 1s， (d) Ni 2p， (e) Co 2p and (f) Mn 2p

In order to clarify the surface elements composition and valences of Pristine, P-LNCM and N3P-LNCM, X-ray photoelectron spectroscopy (XPS) measurements were performed. As shown in Figure 6(a), P, O, Ni, Co, Mn and C elements were detected. In compared the Pristine, the central P 2p peak is detected at 133.5 eV in P-LNCM and

N3P-LNCM samples indicating the presence of phosphate polyanions[40]. It is well

known that XPS could only detect the elements on the surface within about 10 nm[41].

The intensity of the P 2p peak is very weak. Figure 6c shows the O 1s peaks, and the

strong peak corresponding to the lattice oxygen of the layered oxides is located at 529.3

eV for all the samples. But the peaks of Ni2p, Co2p and Mn2p shift to a lower binding

energy in the PO_4^{3-} or Na^+ and PO_4^{3-} incorporated samples, which means that the

bonding of Ni/Co/Mn cations to the anions is weakened by the doping of PO_4^{3-}, or Na^+

and PO_4^{3-}. According to the Table 3, the bond length of TM-O gradually increased in

PO_4^{3-}, or Na^+ and PO_4^{3-} incorporated samples and these results are in accordance with

the XPS results indicating PO_4^{3-} doping or Na^+ and PO_4^{3-} codoping can lead to the

weakening of TM-O covalency. Therefore, small amounts of PO_4^{3-} or Na^+ and PO_4^{3-}

incorporation can modulate the atom bonding environment of the Li-rich layered oxides.
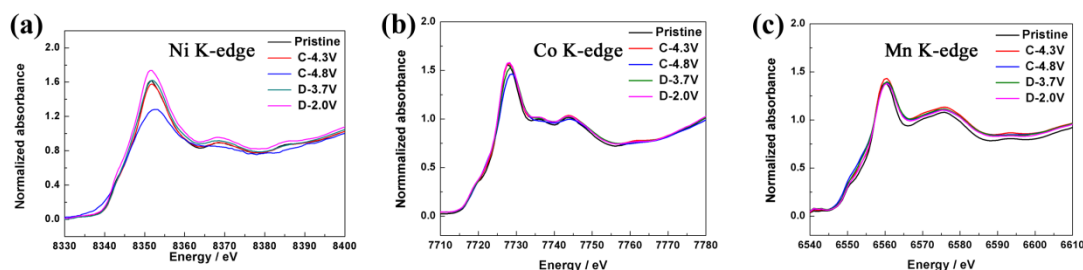

Fig 7 (a) Ni, (b) Co and (c) Mn K-edge XAFS of N3P-LNCM samples at different charge-discharge states.

Fig 7 shows the Ni, Co and Mn K-edge XAFS spectra of N3P-LNCM sample at

different charge-discharge states. The oxidation of the transition metals at different

charge-discharge state was associated to the energy of the spectrum[42-45]. The Ni K-edge

XAFS spectrum in Fig 7(a) indicates that compared with the pristine sample, the energy

of the spectrum shifted to a higher energy when it is charged from 4.3V to 4.8V which

can be attributed to the oxidation of Ni^{2+} to Ni^{3+} and Ni^{3+} to Ni^{4+}, and the energy of the

spectrum gradually shifts to a lower energy when it is discharged from 4.8V to 2.0V

indicating the reduction process of the nickel ions from Ni^{4+} to Ni^{2+} which are in well

agreement with the CV curves(Figure 5). Figure 7(b) shows the Co K-edge XAFS

spectrum, the line peak shifts to the higher energy side slightly when charged to 4.2V,

with further charging to 4.8V, a remarkable shape variation was detected in the spectra

which could be attributed to the oxidation of Co^{3+} to Co^{4+}, and when it discharged from

4.8V to 2.0V, the energy of the spectrum gradually shifts to a lower energy indicates

the reduction of Co^{4+} to Co^{3+}. The Mn K-edge XAFS spectrum shown in Fig 7(c) does

not show an apparent shift, which indicates the valence state of manganese ion is
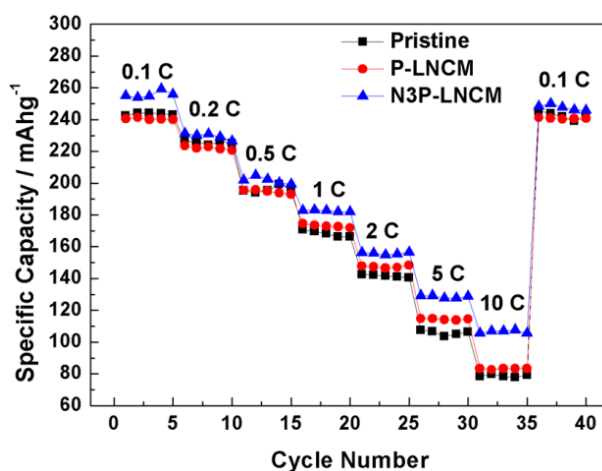
invariant.

Figure 8 Rate capability of pristine, P-LNCM andN3P-LNCM at different rates. 1C=250 mAh g^{-1}

To study the effects of PO_4^{3-} doping and Na^+ and PO_4^{3-} co-doping on the rate

capability of LNCM, the capability of pristine, P-LNCM and N3P-LNCM was tested

under different current densities. The electrochemistry window was set from 2.0 V to

4.8V and the charge-discharge tests was carried out at different current densities of 0.1

C, 0.2 C, 0.5 C, 1 C, 2 C, 5 C, and 10 C (1 C = 250 mAh g^{-1}), respectively. The relative

rate data were summarized in Table 3. All the samples were carried out an activated

procedure at 0.05 C for 2 cycles before the testing. As is shown in Figure 8, the P-LNCM electrode showed a relative lower reversible capacity at 0.1 C and 0.2 C, compared with the pristine sample, but it displays a slightly higher reversible capacity at 1 C, 2 C, 5 C and 10 C. The N3P-LNCM electrode showed a better rate performance than the pristine sample, especially at 10 C, it delivered a discharge capacity of 106.4 mAh g^{-1} while the pristine was only 78.6 mAh g^{-1}. These results indicate that Na^+ and PO_4^{3-} co-doping can improve the high-rate capability of the N3P-LNCM sample which can be largely attributed to the increase of the interslab spacing and the suppression of Li/Ni mixing.

Table 3 Specific capacity of pristine, P-LNCM andN3P-LNCM at different rates

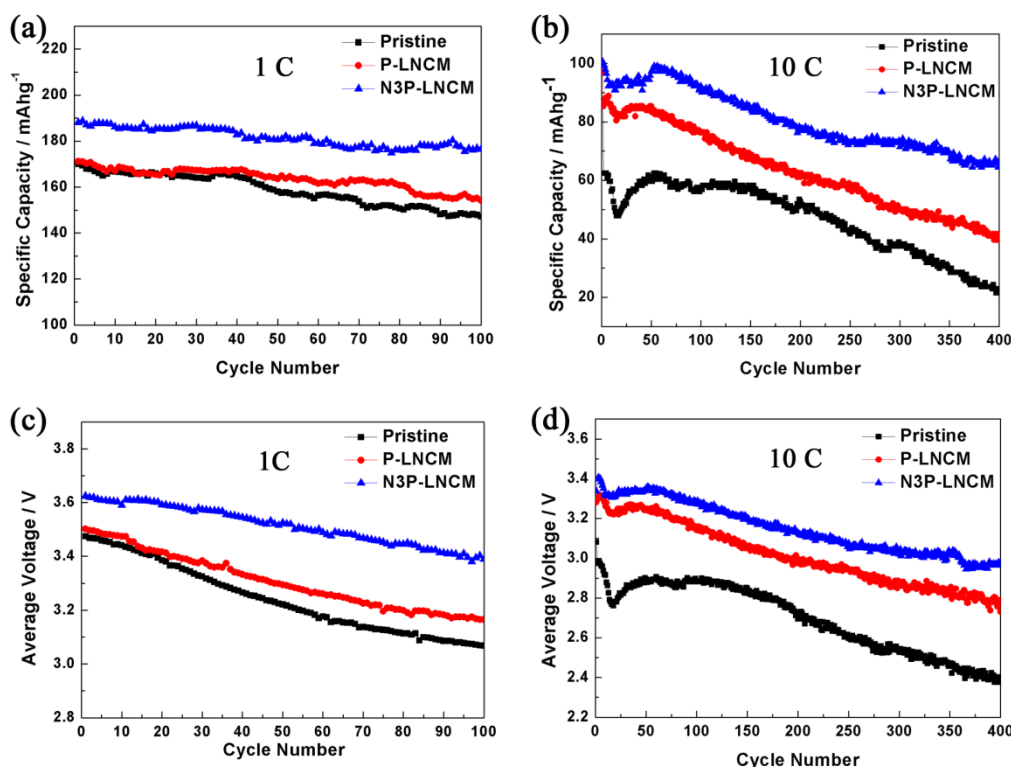| Samples	0.1 C	0.2 C	0.5 C	1 C	2 C	5 C	10 C
Pristine(mAh g^{-1})	243.4	225.5	196.0	168.3	141.4	105.7	78.6
P-LNCM(mAh g^{-1})	210.4	212.1	194.6	173.0	147.4	114.3	83.1
N3P-LNCM(mAh g^{-1})	255.7	229.6	201.6	182.8	155.8	128.5	106.4

Figure 9 The cycling performances of Pristine, P-LNCM and N3P-LNCM at 1 C (a) and 10 C (b). The average discharge voltage of Pristine, P-LNCM and N3P-LNCM at 1 C (c) and 10 C (d)

To further study the effects of PO_4^{3-} doping or Na^+ and PO_4^{3-} co-doping on the cycling performance and the voltage decay, the Pristine, P-LNCM and N3P-LNCM electrodes were cycled at 1 C and 10C between 2.0 V to 4.8 V. Before cycling, the electrodes were activated at 0.05 C for 3 cycles. As is shown in Figure 9a, at the current density of 1 C the initial discharge capacity of the Pristine, P-LNCM and N3P-LNCM sample is 171.5, 171.3 and 188.1 mAh g^{-1}, respectively. After 100 cycles, the Pristine delivers 147.2 mA g^{-1} with a capacity retention of 85.8%. In contrary, after a 100 cycles, the discharge capacity of P-LNCM and N3P-LNCM is 154.2 and 176.5 mAh g^{-1}, respectively, with a capacity retention of 90.0 and 93.8%. At a high current density of 10C, the cycling performance of P-LNCM and N3P-LNCM is much better than the Pristine sample as shown in Figure 9b. At a current density of 10 C, the N3P-LNCM still shows 65.2 mAhg^{-1} with a capacity retention of 64.8% after 400cycles. But the discharge capacity of Pristine electrode sharply decreased to 21.5 mAhg^{-1} with a capacity retention of only 24.8%.

Voltage fading is another critical issue for Li-rich layered oxides cathode materials. As shown in Figure 9c, the discharge medium voltage of Pristine sample decreases from 3.47 to 3.07 V after 100 cycles at current density of 1 C, but for the P-LNCM and N3P-LNCM electrode, it decreases from 3.50 to 3.17 V and 3.62 to 3.39 V, respectively. Figure 9d shows the discharge medium voltage change of these three samples after a 400 cycles at current density of 10 C. It can be clearly seen that the discharge medium voltage of Pristine decreased sharply from 3.08 to 2.39 V, while the voltage decay of P-LNCM and N3P-LNCM electrode was alleviated, especially for the N3P-LNCM

electrode decreases from 3.34 to 2.98 V. It is reported that the voltage fading is mainly caused by the TM cation migration and dissolution which could cause phase transformation from the layered to spinel structure[46]. Therefore, the PO_4^{3-} doping or Na^+ and PO_4^{3-} co-doping could suppress the phase transition and alleviate the voltage fading, which can be attributed to the stabilization of PO_4^{3-} doping on the layered structure.
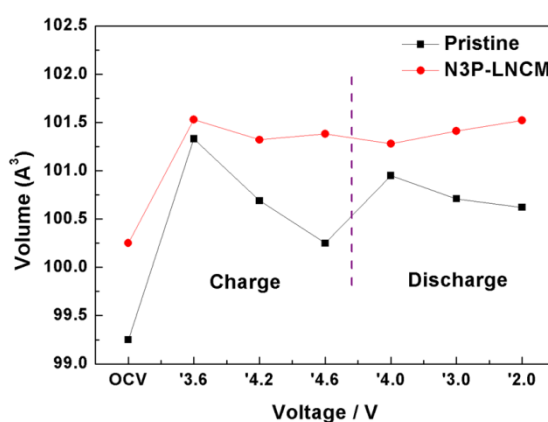

Figure 10 The change of the unit cell volume for Pristine and N3P-LNCM at different charge-discharge states.

To further study how PO_4^{3-} doping improves the stability of the layered structure, we tested the XRD patterns and calculated the volume variation of Pristine and N3P-LNCM electrodes at different charge and discharge states. It has been reported that the decrease of the TM-O covalence could drop the top of the O2p band which results in more stable oxygen ions at high voltage, and the decrease of TM–O covalence during the charge/discharge process are favorable for the stabilization of the layered structure[47-49]. Figure 10 shows the change of the unit cell volume of these two samples during the charge/discharge process. Compared with the Pristine electrode, the variation of unit cell volume is obviously relived after the Na^+ and PO_4^{3-} polyanions co-doping. This result reveals that the decrease of TM-O covalence could mitigate the

lattice change during the charge/discharge process which is favorable to stabilize the layered structure. And the TM-O bond length of N3P-LNCM is decreased which has been verified by the XRD and XPS shown in Table 1 and Figure 6.
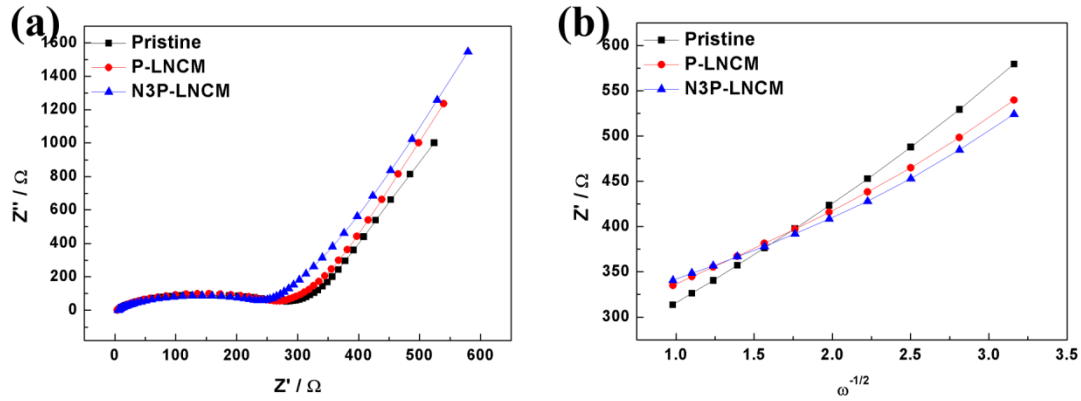

Figure 11 Nyquist plots for Pristine, P-LNCM and N3P-LNCM

The EIS measurement is usually carried out to get further detail information about electrode/electrolyte interface. The charge transfer resistance is reflected by the half circle located in the high frequency range and the Li-ion conductivity (D_{Li}) is reflected by the straight line in the low frequency range reflects[50, 51]. Here we use it to obtain the charge transfer resistance and calculate the Li-ion conductivity of the Pristine, P-LNCM and N3P-LNCM. As shown in Figure 11a, the Rct of the Pristine, P-LNCM and N3P-LNCM is 315, 281 and 279, respectively. We deduce that the significant decrease of the resistance of Rct for P-LNCM and N3P-LNCM is caused by the incorporation of PO_4^{3-} polyanions in the TM layer and Na^+ in the interslab which could enlarge the interslab thickness and stabilize the TM slab. The Warburg constant which is an important constant to influence the Li-ion diffusion (D_{Li}) could be calculated by a linear relationship with *Z' vs $\omega^{-1/2}$* as shown in Figure 11b. Warburg constant for Pristine, P-LNCM and N3P-LNCM is 120.45, 91.78 and 81.84, respectively. The Li-ion diffusion could be calculated by using the following equation: $D_{Li}=1/2[(RT)/(n^2SF^2\sigma C)]^2$, and the

value of R is the gas constant, T is the absolute temperatue, n is the number of the electrons per molecule oxidized, S is the area of electrode, F is the Faraday constant and C is the molar concentration[52, 53]. D_{Li} is calculated to be 5.12×10^{-14}, 8.81×10^{-14} and 1.11×10^{-13} cm^2 s^{-1}, respectively. The results clearly indicate that the N3P-LNCM sample with co-incorporated Na$^+$ and PO$_4^{3-}$ has an enhanced Li-ion conductivity, which could be attributed to the contribution integration of the PO$_4^{3-}$ polyanions in the TM layer and Na$^+$ in the interslab. This is in well agreement with the interlayer spacing expansion and Li/Ni mixing suppression, and high rate performance induced by Na$^+$ and PO$_4^{3-}$ co-doping.

Conclusion

In summary, Na$^+$ and PO$_4^{3-}$ have been successfully co-doped into the Li and TM crystal sites of Li-rich layered oxides cathodes, respectively, using Na$_3$PO$_4$ as a dopant. Compared with the Pristine and the P-LNCM sample, the interslab thickness of N3P-LNCM increased from 2.0912 to 2.1316Å, while the slab thickness decreased from 2.6447 to 2.6058Å. The charge-discharge data demonstrates that the N3P-LNCM doped with Na$^+$ and PO$_4^{3-}$ has a higher rate capacity(106.4 mAhg^{-1} at 10C), excellent capacity retention (93.8%@1C@100 cycles) and the voltage decay has also been mitigated. These enhancements can be attributed to the synergistic effect of Na$^+$ and PO$_4^{3-}$ co-doping. Na$^+$ and PO$_4^{3-}$ co-doping increases the interlayer spacing and suppresses Li/Ni mixing, which facilitate the Li+ diffusion and high-rate performance. In addition, Na$^+$ and PO$_4^{3-}$ co-doping shrinks the thickness of the slabs and weakens the TM-O covalency, which is further favorable to the structure stability and the enhancement of

cycling performance. Thirdly, Na^+ and PO_4^{3-} co-doping also alleviates the volume change during charge-discharge process and stabilizes the layered structure. The proposed integrated strategy of the synergistic doping of foreign elements in different sites can also be used to modulate other cathode materials for lithium-ion batteries.

Acknowledgements

References

1.   B. Dunn, H. Kamath and J.-M. Tarascon, *Science*, 2011, **334**, 928-935.

2.   J. B. Goodenough and Y. Kim, *Chem. Mater.*, 2009, **22**, 587-603.

3.   W. He, D. Yuan, J. Qian, X. Ai, H. Yang and Y. Cao, *J. Mater. Chem. A*, 2013, **1**, 11397-11403.

4.   M. T. McDowell, S. W. Lee, W. D. Nix and Y. Cui, *Adv. Mater.*, 2013, **25**, 4966-4985.

5.   L. Suo, Y.-S. Hu, H. Li, M. Armand and L. Chen, *Nat. Commun.*, 2013, **4**, 1481.

6.   M. Casas-Cabanas, C. Kim, J. Rodríguez-Carvajal and J. Cabana, *J. Mater. Chem. A*, 2016, **4**, 8255-8262.

7.   L. Li, L. Wang, X. Zhang, M. Xie, F. Wu and R. Chen, *ACS Appl. Mater. Inter.*, 2015, **7**, 21939-21947.

8.   R. Shunmugasundaram, R. Senthil Arumugam, K. J. Harris, G. R. Goward and J. Dahn, *Chem. Mater.*, 2015, **28**, 55-66.

9.   M. M. Thackeray, C. Wolverton and E. D. Isaacs, *Energ. Environ. Sci.*, 2012, **5**, 7854-7863.

10.   F. Zhou, X. Zhao, A. van Bommel, X. Xia and J. Dahn, *J. Electrochem. Soc.*, 2011, **158**, A187-A191.

11.   H. Yu, R. Ishikawa, Y. G. So, N. Shibata, T. Kudo, H. Zhou and Y. Ikuhara, *Angew. Chem. Inter. Edit.*, 2013, **52**, 5969-5973.

12.   J. Rana, R. Kloepsch, J. Li, T. Scherb, G. Schumacher, M. Winter and J. Banhart, *J. Mater. Chem. A*, 2014, **2**, 9099-9110.

13.   A. R. Armstrong, M. Holzapfel, P. Novák, C. S. Johnson, S.-H. Kang, M. M. Thackeray and P. G. Bruce, *J. Am. Chem.Soc.*, 2006, **128**, 8694-8698.

14.   H. Koga, L. Croguennec, M. Ménétrier, K. Douhil, S. Belin, L. Bourgeois, E. Suard, F. Weill and C. Delmas, *J. Electrochem. Soc.*, 2013, **160**, A786-A792.

15.   M. Sathiya, A. M. Abakumov, D. Foix, G. Rousse, K. Ramesha, M. Saubanère, M. Doublet, H. Vezin, C. Laisa and A. Prakash, *Nat. Mater.*, 2015, **14**, 230-238.

16.   M. Bettge, Y. Li, K. Gallagher, Y. Zhu, Q. Wu, W. Lu, I. Bloom and D. P. Abraham, *J. Electrochem. Soc.*, 2013, **160**, A2046-A2055.

17.   G. Singh, R. Thomas, A. Kumar and R. Katiyar, *J. Electrochem. Soc.*, 2012, **159**, A410-A420.

18.   D. Arumugam, G. P. Kalaignan and P. Manisankar, *J. Solid State Electr.*, 2009, **13**, 301-307.

19.	V. Subramanian and G. T.-K. Fey, *Solid State Ionics*, 2002, **148**, 351-358.

20.	G. Fey, J. Chen, V. Subramanian and T. Osaka, *J. Power Sources*, 2002, **112**, 384-394.

21.	B. Li, H. Yan, J. Ma, P. Yu, D. Xia, W. Huang, W. Chu and Z. Wu, *Adv. Funct. Mater.*, 2014, **24**, 5112-5118.

22.	H.-Z. Zhang, F. Li, G.-L. Pan, G.-R. Li and X.-P. Gao, *J. Electrochem. Soc.*, 2015, **162**, A1899-A1904.

23.	H. Zhang, Q. Qiao, G. Li and X. Gao, *J. Mater. Chem. A*, 2014, **2**, 7454-7460.

24.	Y. Zhao, J. Liu, S. Wang, R. Ji, Q. Xia, Z. Ding, W. Wei, Y. Liu, P. Wang and D. G. Ivey, *Adv. Funct. Mater.*, 2016, **26**, 4760-4767.

25.	W. Yuan, H. Zhang, Q. Liu, G. Li and X. Gao, *Electrochim. Acta*, 2014, **135**, 199-207.

26.	M.-S. Park, J.-W. Lee, W. Choi, D. Im, S.-G. Doo and K.-S. Park, *J. Mater. Chem.*, 2010, **20**, 7208-7213.

27.	Y. K. Sun, M. J. Lee, C. S. Yoon, J. Hassoun, K. Amine and B. Scrosati, *Adv. Mater.*, 2012, **24**, 1192-1196.

28.	X. Zhang, C. Yu, X. Huang, J. Zheng, X. Guan, D. Luo and L. Li, *Electrochim. Acta*, 2012, **81**, 233-238.

29.	Z.-Y. Li, R. Gao, J. Zhang, X. Zhang, Z. Hu and X. Liu, *J. Mater. Chem. A*, 2016, **4**, 3453-3461.

30.	Y. Wang, Z. Yang, Y. Qian, L. Gu and H. Zhou, *Adv. Mater.*, 2015, **27**, 3915-3920.

31. J. Zhang, Z. Li, R. Gao, Z. Hu and X. Liu, *J. Phys. Chem. C*, 2015, **119**, 20350-20356.

32. L. Croguennec, J. Bains, J. Bréger, C. Tessier, P. Biensan, S. Levasseur and C. Delmas, *J. Electrochem. Soc.*, 2011, **158**, A664-A670.

33. M. Guilmard, A. Rougier, M. Grüne, L. Croguennec and C. Delmas, *J.Power Sources*, 2003, **115**, 305-314.

34. D. Xie, G. Li, Q. Li, C. Fu, J. Fan and L. Li, *Electrochim. Acta*, 2016, **196**, 505-516.

35. S. Ramakumar, C. Deviannapoorani, L. Dhivya, L. S. Shankar and R. Murugan, *Prog. Mater. Sci.*, 2017, 88, 325-411.

36. O. Dolotko, A. Senyshyn, M. Mühlbauer, K. Nikolowski and H. Ehrenberg, *J. Power Sources*, 2014, **255**, 197-203.

37. Y. X. Wang, K. H. Shang, W. He, X. P. Ai, Y. L. Cao and H. X. Yang, *ACS Appl. Mater. Inter.*, 2015, **7**, 13014-13021.

38. Z. Lu and J. R. Dahn, *Journal of The Electrochem. Soc.*, 2002, **149**, A815-A822.

39. W. He, J. Qian, Y. Cao, X. Ai and H. Yang, *RSC Adv.*, 2012, **2**, 3423-3429.

40. E. Markevich, R. Sharabi, H. Gottlieb, V. Borgel, K. Fridman, G. Salitra, D. Aurbach, G. Semrau, M. Schmidt and N. Schall, *Electrochem. Commun.*, 2012, **15**, 22-25.

41. B. Philippe, R. m. Dedryvère, J. Allouche, F. Lindgren, M. Gorgoi, H. k. Rensmo, D. Gonbeau and K. Edström, *Chem. Mater.*, 2012, **24**, 1107-1115.

42. H. Konishi, T. Hirano, D. Takamatsu, A. Gunji, X. Feng and S. Furutsuki,

Electrochim. Acta, 2015, **186**, 591-597.

43.   Y. Koyama, I. Tanaka, H. Adachi, Y. Makimura and T. Ohzuku, *J. Power Sources*, 2003, **119-121**, 644-648.

44.   D. Mori, H. Kobayashi, T. Okumura, H. Nitani, M. Ogawa and Y. Inaguma, *Solid State Ionics*, 2016, **285**, 66-74.

45.   T. Nonaka, C. Okuda, Y. Seno, H. Nakano, K. Koumoto and Y. Ukyo, *J. Power Sources*, 2006, **162**, 1329-1335.

46.   A. Boulineau, L. Simonin, J.-F. o. Colin, E. Canévet, L. Daniel and S. b. Patoux, *Chem. Mater.*, 2012, **24**, 3558-3566.

47.   D. Ye, G. Zeng, K. Nogita, K. Ozawa, M. Hankel, D. J. Searles and L. Wang, *Adv. Funct. Mater.*, 2015, **25**, 7488-7496.

48.   B. Song, S. J. Day, T. Sui, L. Lu, C. C. Tang and A. M. Korsunsky, *Phys. Chem. Chem. Phys.*, 2016, **18**, 4745-4752.

49.   C.-H. Shen, S.-Y. Shen, F. Fu, C.-G. Shi, H.-Y. Zhang, M. J. Pierre, H. Su, Q. Wang, B.-B. Xu and L. Huang, *J. Mater. Chem. A*, 2015, **3**, 12220-12229.

50.   Z. Li, F. Du, X. Bie, D. Zhang, Y. Cai, X. Cui, C. Wang, G. Chen and Y. Wei, *J. Phys. Chem. C*, 2010, **114**, 22751-22757.

51.   N. Takami, A. Satoh, M. Hara and T. Ohsaki, *J. Electrochem. Soc.*, 1995, **142**, 371-379.

52.   L. Li, Z. Chen, Q. Zhang, M. Xu, X. Zhou, H. Zhu and K. Zhang, *J. Mater. Chem. A*, 2015, **3**, 894-904.

53.   D. Luo, G. Li, C. Fu, J. Zheng, J. Fan, Q. Li and L. Li, *Adv. Energy Mater.*, 2014,

4.1400062